Dual Li-ion migration channels in an ester-rich copolymer/ionic liquid quasi-solid-state electrolyte for high-performance Li-S batteries

Dual Li-ion migration channels in an ester-rich copolymer/ionic liquid quasi-solid-state electrolyte for high-performance Li—S batteries†

Xiaomin Cai,[a] Bei Ye,a Jianlong Ding,[a] Ziyun Chi,[a] Liping Sun,[a] Petr Saha[b] and Gengchao Wang Q*[a]

[a]*Shanghai Key Laboratory of Advanced Polymeric Materials, Shanghai Engineering Research Center of Hierarchical Nanomaterials, School of Materials Science and Engineering, East China University of Science and Technology, P.O. Box 289, 130 Meilong Rd., Shanghai 200237, P. R.China. E-mail: gengchaow@ecust.edu.cn; Tel: +86-21-64253527*

[b]*Centre of Polymer Systems, University Institute, Tomas Bata University, Tr. T. Bati 5678, Zlin-76001, Zlín, Czech Republic*

Introduction

In recent years, lithium-sulfur batteries are considered to be some of the most promising candidates to meet the energy storage needs for electric vehicles and portable electronic devices,[1-4] due to their high theoretical energy density of 2600 W h kg^{-1}, low cost, abundant storage, and environmental friendliness.[5-8] At present, the research on lithium-sulfur batteries is mainly focused on solving problems related to active materials,[9-11] and great progress has been made in energy density, power density and cycle life.[12-14] However, despite the great achievements of lithium-sulfur batteries based on liquid electrolytes, their electrochemical and thermal instability still bring potential safety hazards.[15-19] Therefore, there is an urgent need to construct a solid-state electrolyte[20-22] with high ionic conductivity, long-term stable interface, and excellent electrochemical stability to replace liquid electrolytes.[23-26]

Recently, various solid electrolytes including polymer elec-trolytes[27-29] and ceramic electrolytes (mainly based on oxides, sulfides and their derivatives)[30-33] have been reported for solid-state lithium-sulfur batteries. Among them, solid polymer electrolytes (SPEs) have attracted much attention due to their non-volatility, low flammability, no electrolyte leakage, easy processing, and high mechanical strength.[34] At present, the research on SPEs mainly focuses on how to improve their room temperature ionic conductivity.[35,36] For example, Li et al.[37] used the solvent casting method to incorporate Li10SnP2S12 into a PEO matrix, and the ionic conductivity of the composite polymer electrolyte at 50 °C reached 1.69 x 10^{-4} S cm^{-1}.

In addition, since the solid polymer electrolyte usually has a certain mechanical strength, the solid-solid contact between it and the solid electrode is inherently poor.[11,25,38,39] During electrochemical cycling, the irreversible volume change of the electrode material will produce a large stress at the interface, which will undoubtedly worsen the situation.[40-44] Fan et al.[45] used atomic deposition to coat Al2O3 on the surface of polyethylene oxide-lithium-bis(trifluoromethylsulfonyl)imide to construct a stable solid-solid interface.

However, the challenges faced by lithium-sulfur batteries are more than just interface issues. Since there is no liquid, once lithium polysulfides shuttle it will be a completely irreversible process.[40] Xia et

al.[46] prepared a SPE with a threedimensional structure by UV polymerization. The presence of electron-donating groups successfully inhibited the shuttle of polysulfides. At high current density, the overpotential increases sharply, the charge distribution changes, and lithium dendrites grow rapidly.[35,43,47-49] Cui et al.[50] used a mixture of Cu_3N and styrene-butadiene rubber (SBR) to construct an artificial SEI layer. The high modulus coating effectively inhibited the nucleation growth of lithium dendrites. Therefore, in general, the challenges faced by solid polymer electrolytes include increasing ionic conductivity, improving interface problems, enhancing mechanical properties, and inhibiting sulfur shuttle and lithium dendrites.[11,39,51,52]

Herein, ester-rich poly(vinyl carbonate-co-butyl acrylate) (P(VCA-co-BA)) copolymers were prepared by radical polymerization. On this basis, in order to further improve the room temperature ionic conductivity of the SPE, we introduced 1-ethyl-3-methylimidazolium bis[(trifluoromethyl)sulfonyl]imide ([EMIM]TFSI) ionic liquid to enrich the free mobile ions in the system and increase the number of "effective ions". There are dual Li-ion migration channels in the system. One is the movement of chain segments to drive ion transmission, and the other is rapid ion exchange between lithium ions and the ionic liquids. Furthermore, the [EMIM]TFSI realizes a "soft contact" between the electrolyte and the electrode. The assembled Li// SPE-IL//Li battery has a high critical current density (CCD) value of 3.8 mA cm^{-2} at room temperature. There is close overlap between the carbon nanotubes in the nitrogen-doped self-supporting sulfur cathode and the electrolyte membrane. These work together to stabilize the interface engineering in lithium-sulfur batteries. The results show that the SPE-IL-based quasi-solid-state lithium-sulfur battery exhibits a high degree of reversibility at 60 °C, and the first discharge capacity reaches 1106 mA h g^{-1}. The average capacity decay per cycle during 300 cycles is only 0.066%.

Experimental section

Preparation of P(VCA-co-BA) copolymers

Poly(vinyl carbonate-co-butyl acrylate) (P(VCA-co-BA)) copolymers were prepared by radical polymerization. A certain molar ratio (VCA : BA = 2 : 1, 3 : 1, 4 : 1, 5 : 1) of vinylene carbonate (VC, Aladdin, China) and butyl acrylate (BA, Aladdin, China) was taken in a round bottom flask, 0.5 wt% BPO was added, and dissolved using ultrasound. The polymerization was initiated by heating and stirring in a water bath at 80 °C. Then the viscous liquid was poured into a glass plate mold and put in an oven at 80 °C for 10 h, and the temperature was raised to 100 °C for 2 h to obtain the copolymer. P(VCA-co-BA) was dissolved in N,N-dimethylacetamide (DMAC), and a precipitate was obtained by adding excess methanol. The operation was repeated twice, and finally dried to obtain pure P(VCA-co-BA).

Preparation of P(VCA-co-BA)/LiTFSI/[EMIM]TFSI ternary electrolytes

P(VCA-co-BA), bistrifluoromethanesulfonimide lithium salt (LiTFSI, Aladdin) and 1-ethyl-3-methylimidazolium bis[(tri-fluoromethyl)sulfonyl]imide ([EMIM]TFSI, Aladdin) were taken in a certain ratio, DMAC solvent was added, and the flask was stirred at 60 °C until the components dissolved. Then the liquid was poured into a polytetrafluoroethylene plate, the solvent was removed in an oven at 60 °C, and then dried in a vacuum at 100 °C to obtain the P(VCA-co-BA)/LiTFSI/[EMIM]TFSI electrolyte (SPE-IL). The preparation method of the P(VCA-co-BA)/ LiTFSI electrolyte (SPE) is the same as above, except that no [EMIM]TFSI ionic liquid is added.

Preparation of N(PDA)-CNT@S flexible self-supporting cathodes

First, carbon nanotube (CNT) films (Suzhou Jedi Nanotechnology Co., Ltd., China) were put into ethanol and treated with ultrasound. Then they were immersed in 0.01 M Tris-HCl buffer solution (25 mL of 0.1 mol L^{-1} tris(hydroxymethyl)-amino-methane solution was mixed with 7.3 mL of 0.1 mol L^{-1} hydrochloric acid solution and diluted to 250 mL), and then dopamine (DA) powder was added to the solution (with DA concentrations of 0, 0.2, 1.0 and 1.4 mg mL^{-1}) and ultra-sonicated for 30 min. After bubbling at room temperature for 24 h, the PDA modified CNT films were taken out and washed with deionized water. Then they were freeze-dried for 10 h to obtain PDA-coated carbon nanotubes (PDA-CNT). The PDA-CNT films were heated to 800 °C in a tube furnace at a heating rate of 2 °C min^{-1} and kept for 2 h to obtain N(PDA)-CNT.

The carbonized N(PDA)-CNT films were loaded with sulfur by electrochemical oxidation in 0.2 M Na2S solution. N(PDA)-CNT was used as the working electrode, and Pt as the counter electrode and reference electrode. S2- is oxidized to elemental sulfur at a constant potential of 1.25 V, and the amount of charge was controlled at 30C. The sulfur loaded N(PDA)-CNT films were repeatedly washed with deionized water to remove residual ions. After freeze-drying for 3 h, they were placed in a hydrothermal kettle and heat treated in an oven at 155 °C for 12 h. Finally, they were dried in a vacuum oven at 60 °C for 24 h to obtain N(PDA)-CNT@S cathodes.

Assembling the battery

Blocking electrode symmetrical cells. Both the working electrode and the counter electrode are stainless steel sheets with a diameter of 15 mm and a thickness of 0.5 mm, which are used to test the ionic conductivity.

Li-Li symmetrical cells. Both the working electrode and the counter electrode are lithium sheets. A lithium sheet, polymer electrolyte membrane and lithium sheet were assembled into CR2025 cells successively and packaged.

Li-S battery. N(PDA)-CNT@S, P(VCA-co-BA)/LiTFSI/[EMIM] TFSI and a lithium sheet are used as the cathode, electrolyte and anode, respectively, to assemble Li-S batteries. All batteries are assembled in a glove box with water and oxygen levels below 0.1 ppm.

Characterization and electrochemical measurements

Fourier transform infrared (FTIR) spectroscopy was performed using a Nicolet 6700 spectrometer. 1H-NMR was carried out using a Brooke's superconducting Fourier transform NMR spectrometer (400 MHz/AVANCE III 400). The morphology of the samples was characterized by field emission scanning electron microscopy (FE-SEM, Hitachi S-4800). Raman spectra were collected with a Renishaw inVia Raman spectrometer system. X-ray diffraction (XRD) was performed using a Rigaku D/Max 2550 VB/PC X equipped with a Cu target X-ray tube. X-ray photoelectron spectroscopy (XPS, ESCALAB 250Xi, Thermo Scientific) with an Al Ka X-ray source was performed. Thermogravimetric (TG) analysis was performed on a TG instrument (STA409PC) at a heating rate of 10 0C min^{-1} under a N_2 atmosphere. Dynamic thermomechanical analysis (DMA) was carried out on a TA DMA Q800. Differential scanning calorimetry (DSC) was performed on a modulated DSC2910 (USA). The molecular weight distribution was measured using a gel permeation chromatograph (PL-GPC50 type), where the solvent was DMF, and polystyrene was used as the standard substance with a flow rate of 1 mL min^{-1}. The polymer film was cut into a 50 x 4 mm spline using a dumbbell cutter, and its tensile properties were tested using a universal tensile testing machine at a stretching speed of 25 mm min^{-1}.

The ionic conductivity (s) of the polymer electrolytes was measured by AC impedance spectroscopy using a CHI 760C electrochemical workstation in the frequency range from 100 kHz to 0.01 Hz with an AC amplitude of 5 mV. And the value can be estimated using the equation s = 1/(Rb x A), where l is the thickness (cm) of the membrane, Rb is the bulk resistance (U) obtained from the first intercept on the c-axis of the impedance figures, and A is the contact area (cm^2) of the membrane with the current collector.

The galvanostatic charge/discharge test was carried out on a LAND CT2001A battery tester between 1.8 and 2.7 V (versus Li/ Li^+). Electrochemical impedance spectroscopy (EIS) (frequency range: 0.01-100 kHz; amplitude: 5 mV) was conducted on a CHI 760E electrochemical workstation.

Results and discussion

As shown in Fig. 1a, P(VCA-co-BA) was prepared by radical polymerization using vinylene carbonate (VCA) and butyl acrylate (BA) monomers. FTIR analysis (Fig. S1f) and ^{1}H NMR (Fig. S2a and bf)/^{13}C NMR (Fig. S2cf) spectra prove that the two monomers are successfully polymerized.

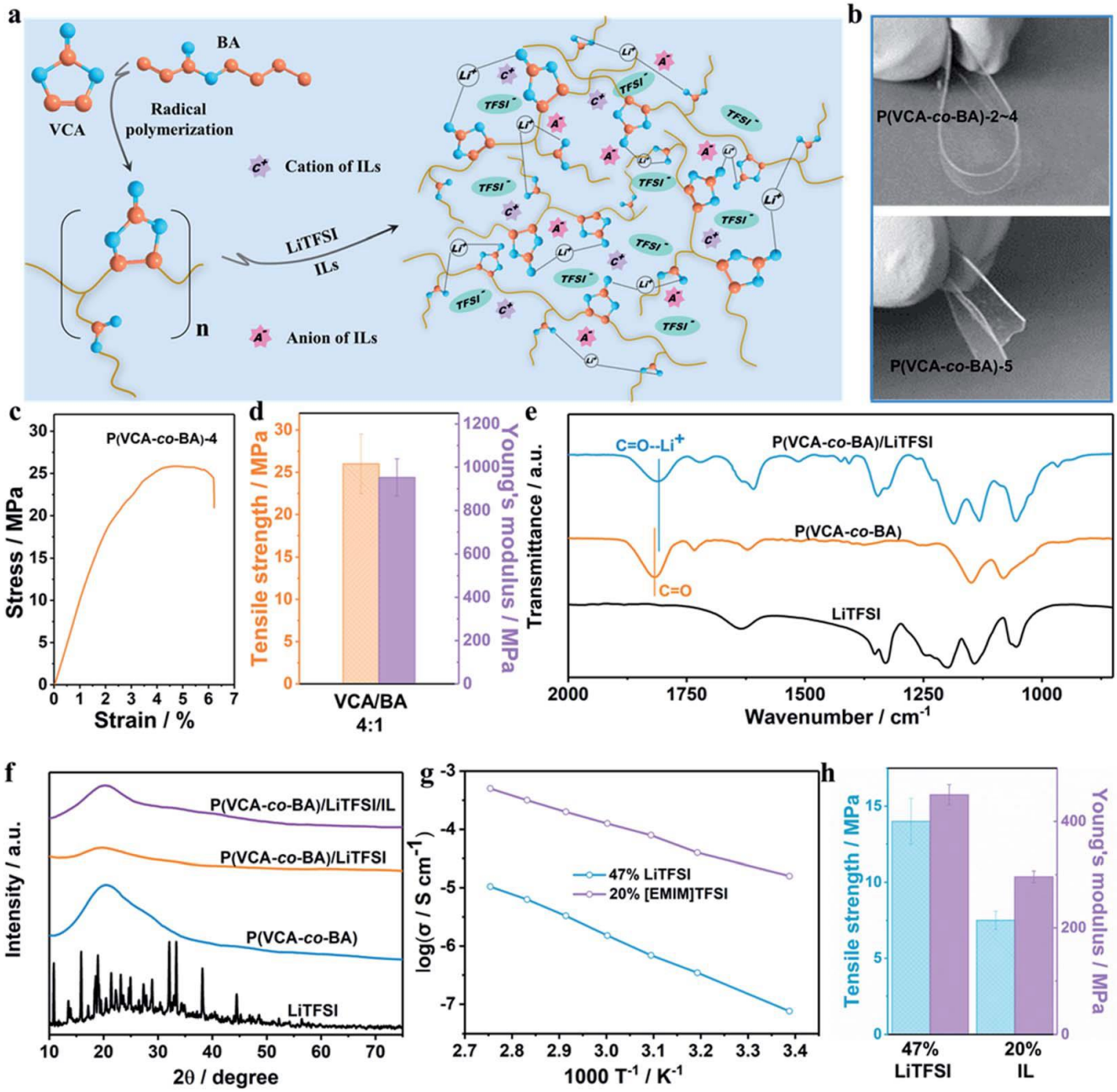

Fig. 1 (a) Preparation route of P(VCA-co-BA)/LiTFSI/IL SPE-IL polymer electrolytes. (b) Digital photos of P(VCA-co-BA) with various VCA/BA feed ratios in the bending state. (c) Stress-strain curve and (d) tensile strength/Young's modulus of P(VCA-co-BA)-4. (e) FTIR spectra of LiTFSI, P(VCA-co-BA) and P(VCA-co-BA)/LiTFSI. (f) XRD patterns of LiTFSI, P(VCA-co-BA), P(VCA-co-BA)/LiTFSI and P(VCA-co-BA)/LiTFSI/IL. (g) Ion conductivity-temperature curves and (h) tensile strength/Young's modulus of the SPE with 47 wt% LiTFSI and 20 wt% [EMIM]TFSI.

There are abundant free mobile ions in the system after the introduction of the ionic liquids [EMIM]TFSI and LiTFSI, which is very beneficial to improve the ion transport kinetics. The rigid-flexible molecular structure of P(VCA-co-BA) is expected to solve the brittleness problem of PVCA.[53] Fig. 1b shows the photos of P(VCA-co-BA) with different monomer feeding ratios after 180° bending. When the ratios of VCA/BA are 2/1, 3/1 and 4/1, it can be seen that P(VCA-co-BA)-2-4 inherits the flexibility of BA, showing a soft state and can be bent at will. However, when continuing to increase the ratio of VCA/BA to 5/1, P(VCA-co-BA)-5 loses its flexibility, showing the brittleness of VCA and breaking off immediately. The stress-strain curves in Fig. 1c and S3af were used to evaluate the mechanical properties of P(VCA-co-BA). When the ratio of VCA/BA was increased to 3/1, the tensile strength suddenly increased to 20 MPa. When continuously increasing the amount of VCA, the tensile strengths of P(VCA-co-BA)-4 and P(VCA-co-BA)-5 were 25.8 and 27.4 MPa, respectively, with no obvious difference. This result was revealed by 1H-NMR (Fig. S2af) and GPC (Fig. S4 and Table S1f) analysis. From the calculation in Fig. S2a, † it is known that the compositions of VCA/BA in P(VCA-co-BA)-4 and P(VCA-co-BA)-5 are 2.8/1 and 3/1, respectively, and their molecular weight and PDI are close. Therefore, the tensile strength, Tg, and tan 5 of P(VCA-co-BA)-4 and P(VCA-co-BA)-5 are almost the same (Fig. S5†).

The development of a high-modulus electrolyte film can inhibit the growth of lithium dendrites and prevent the lithium dendrites from penetrating the electrolyte, so as to improve the safety of the battery.[54,55] As shown in Fig. 1d and S3b,† Young's modulus and tensile strength show the same change trend. Compared with the 260 MPa of P(VCA-co-BA)-2, the Young's modulus of P(VCA-co-BA)-3 is increased almost twice. Furthermore, for P(VCA-co-BA)-4 and P(VCA-co-BA)-5, the levels are close to 'GPa', i.e. 952 and 987 MPa, respectively. Through comprehensive consideration, P(VCA-co-BA)-4 with excellent flexibility and mechanical properties was selected for further study.

The polymer electrolytes of P(VCA-co-BA)/LiTFSI were prepared by the method of solvent film-forming. In order to study the dissociation state of Li^+ in the P(VCA-co-BA)/LiTFSI electrolyte, the FTIR spectra of P(VCA-co-BA), LiTFSI, and P(VCA-co-BA)/LiTFSI electrolyte were compared. It can be seen from Fig. 1e that after adding LiTFSI to P(VCA-co-BA), the characteristic band of the C=O stretching vibration for the P(VCA-co-BA)/LiTFSI electrolyte red-shifts from 1817 cm^{-1} to 1811 cm^{-1}, which means that there is an interaction between Li^+ and C=O in P(VCA-co-BA). In addition, the crystallization degree of the electrolyte was studied by XRD as shown in Fig. 1f. The results show that the amorphous polymer P(VCA-co-BA) has a wide dispersion peak near 20° while the LiTFSI white crystalline powder has several characteristic diffraction peaks. The crystal diffraction peak of LiTFSI disappears after adding LiTFSI and [EMIM]TFSI to the P(VCA-co-BA) polymer electrolyte. This further proves that the crystallization of LiTFSI is suppressed by the interaction between the LiTFSI and the P(VCA-co-BA).

The ionic conductivity is a key index of whether the electrolyte can be used in batteries. With the addition of LiTFSI, the room temperature ionic conductivity of P(VCA-co-BA)/LiTFSI increases continuously (Fig. S6a†). However, when the content of LiTFSI reaches 39 wt%, the increase rate of conductivity slows down. The ionic conductivity behavior of solid polymer electrolytes is directly related to the movement of polymer chain segments.[56,57] As can be seen in Fig. 1g and S8a,† the dependence of ionic conductivity on temperature basically conforms to the VTF equation.[58] In addition, considering the effect of the LiTFSI content on the mechanical properties of the electrolyte membrane

(Fig. 1h and S6b†), the optimal condition is 47 wt% LiTFSI content with excellent ionic conductivity and tensile strength/Young's modulus, meeting the use demand.

As shown in Fig. S7a,† when the [EMIM]TFSI content reaches 30 wt%, the room temperature ionic conductivity is as high as 1.1 x 10^{-4} S cm^{-1}, which is three orders of magnitude higher than that of P(VCA-co-BA)/LiTFSI. When 20 wt% ionic liquid is added, the ionic conductivity is increased by an order of magnitude than when 15 wt% is added. When it continues to increase to 25 wt%, the conductivity is only doubled compared to that of 20 wt%, and at this time, the Young's modulus dropped below 200 MPa. In addition, the effects of 15 wt%, 20 wt%, and 25 wt% ionic liquid addition on stable interface construction were compared. It can be seen from the impedance spectra (Fig. S9f) of the Li//SPE-IL//Li cells that when 20 wt% ionic liquid is added, the "soft contact" is successfully built, which almost coincides with the curve of 25 wt% ionic liquid content. Fig. 1g and S8bf show the temperature dependence of ionic conductivity with different [EMIM]TFSI contents, and it is found that it still conformed to the VTF equation, which is consistent with the change rule of SPEs without ionic liquids. This shows that the introduction of ionic liquids did not disturb the original ionic conduction path in the system. Considering the tensile strength/Young's modulus of quasisolid-state electrolytes with different [EMIM]TFSI contents (Fig. 1h and S7b†), ionic conductivity, stable interface construction and cost factors, the SPE-IL with an [EMIM]TFSI content of 20 wt% was selected for further study.

There are two Li-ion transport channels in the system (Fig. 2). In the conduction process of lithium ions in the polymer, first, the lithium ion interacts with certain active groups on the polymer chain segment to form an association complex. With the movement of polymer chain segments, these active centers involved in the association continue to move or replace, thereby realizing Li-ion conduction.[59] In P(VCA-co-BA)/LiTFSI, Li^+ relies on "association-disassociation" with carbonyl groups to move together with polymer segments. Furthermore, the solubilization effect of ionic liquids introduces a new ion transport channel, that is, rapid ion exchange between lithium ions and ionic liquids.[60] For the imidazole ionic liquid [EMIM] TFSI, the transmission number t (t — $D_+/(D_+ + D\_)$, where D is the diffusion coefficient of the anion and cation) is greater than 0.5, which means that imidazole cations always diffuse faster than anions.[61] $[EMIM]^+$ always arrives at the solid-phase interface faster, and the mass transfer process between the solid and liquid phases occurs, that is, the ion exchange between [EMIM]+ and Li^+. The so-called ion exchange is the diffusion process of a substance between the liquid phase and the solid phase.[62]

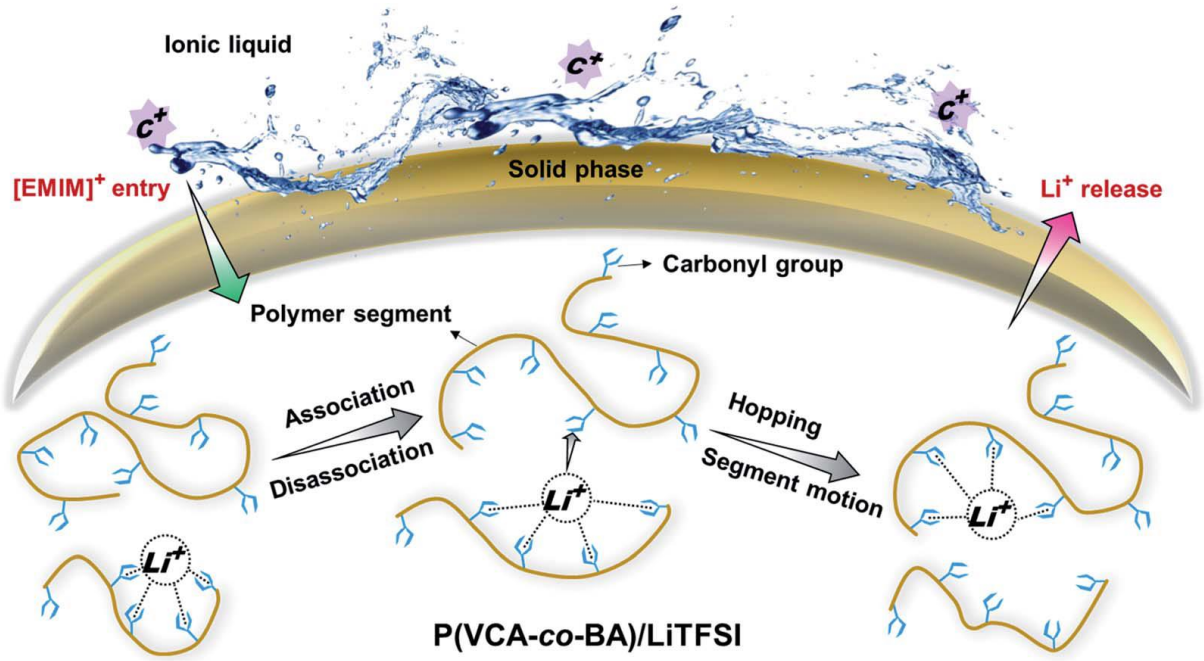

Fig. 2 Schematic diagram of dual Li-ion migration channels for the SPE-IL.

This process is a reversible equivalent exchange reaction, which means that an $[EMIM]^+$ entering the solid phase will be accompanied by the release of a Li^+ to the liquid phase.[63] The ATR-FTIR result shows that the characteristic band corresponding to the carbonate groups changes from 1811 in the SPE to 1815 cm^{-1} in the SPE-IL (Fig. 1e and S10†). This confirms that the $[EMIM]^+$ diffused from the liquid phase to the solid phase to replace Li^+, and the bond between the carbonyl group and Li^+ is relatively weakened.

In addition to improving ionic conductivity, the introduction of ionic liquids is expected to improve the stability of the interface between the electrode and the electrolyte. As shown in Fig. 3a, the migration and deposition of lithium ions in liquid electrolytes are disorderly, which promotes the nucleation and growth of lithium dendrites.

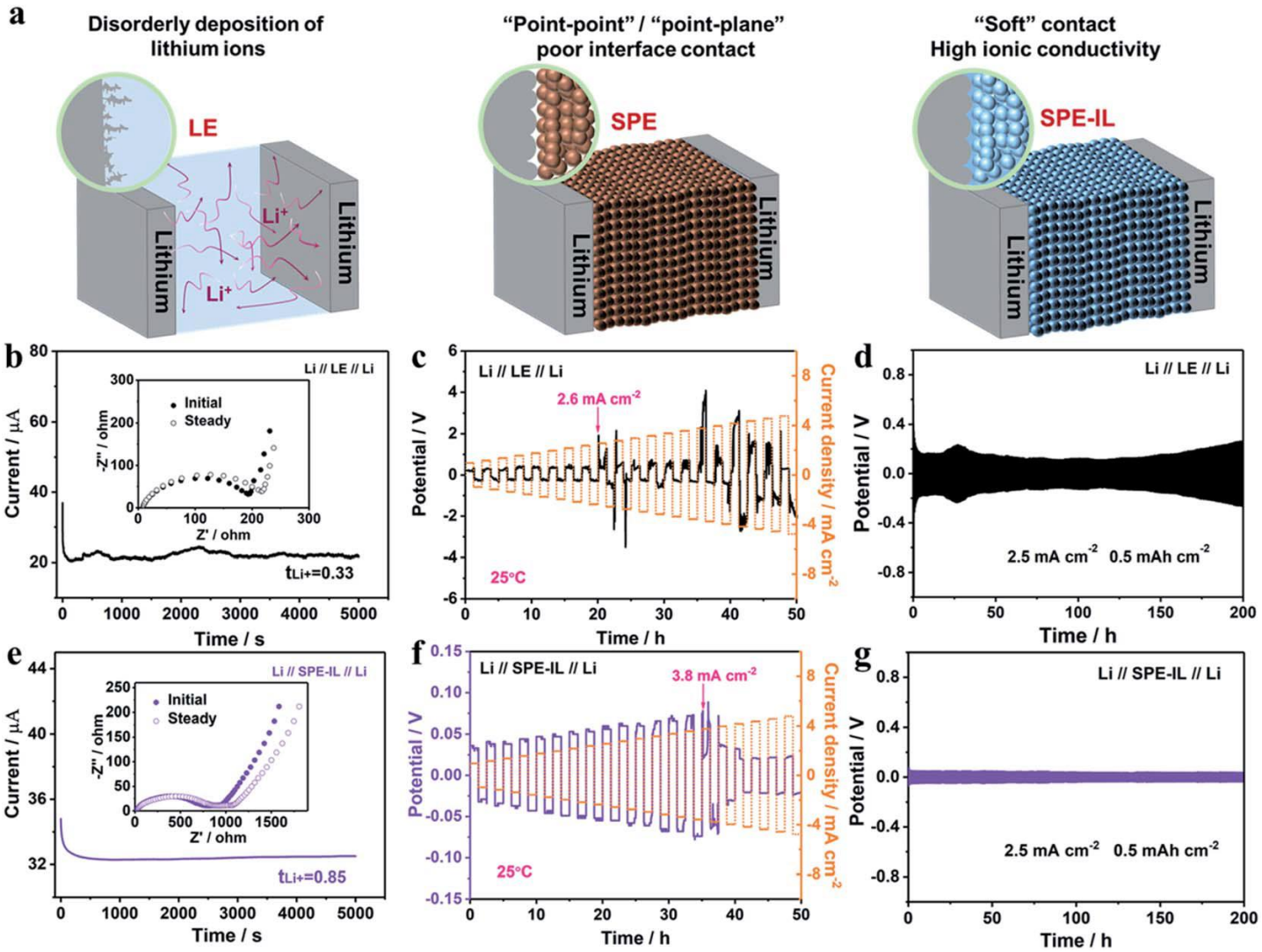

Fig. 3 (a) Schematic diagram of the interfacial contact. (b) Impedance spectra and DC polarization curve, (c) the cycle curve when the current density increases gradually, and (d) 500 h long-term cycle curve of the Li//LE//Li cell at 25 °C. (e) Impedance spectra and DC polarization curve, (f) the cycle curve when the current density increases gradually, and (g) 500 h long-term cycle curve of the Li//SPE-IL//Li cell at 25 °C

The SPE is different from the solid-liquid contact interface of the liquid electrolyte. The "point-point"/"point-plane" contact between the electrode and the electrolyte makes the interface contact resistance very large (Fig. S11†). The introduction of ionic liquids in the SPE-IL realizes the "soft contact" between the electrode and the electrolyte, and promotes the formation of a stable interface.

For qualified polymer electrolytes, as an indicator of ion transport performance, the Li-ion transfer number (tLi^+) is as important as the ionic conductivity. The increase of tLi^+ is one of the necessary conditions to alleviate electrode polarization and slow capacity attenuation. According to the AC impedance and the DC polarization data in Fig. 3b and e, the tLi^+ of the P(VCA-co-BA)/LiTFSI/[EMIM]TFSI ternary polymer electrolyte is calculated to be as high as 0.85 using the Bruce-Vincent equation.[64,65] tLi+ close to 1 can effectively inhibit the generation of lithium dendrites.[66] This is attributed to the synergistic effect of dual Li-ion migration modes (Fig. 3a), polymer segment motion and ion exchange with ionic liquids, which promotes the increase of tLi^+.

The ability of the SPE-IL to inhibit lithium dendrites was evaluated by assembling lithium-symmetric batteries and performing electrochemical cycles at room temperature. As shown in Fig. 3c and f, the current density was set from 1 mA cm^{-2} to 10 mA cm^{-2} in steps of 0.2 mA cm^{-2}. With the increase of

current density in the form of an arithmetic sequence, the voltage also increases regularly. However, at a current density of 3.8 mA cm^{-2}, the voltage suddenly fluctuates, and the current density at this time corresponds to the critical current density (CCD) of lithium dendrites formed in Li//SPE-IL//Li. In comparison, the CCD value of the Li//SPE//Li battery in Fig. 3c is only 2.6 mA cm^{-2}. Furthermore, Fig. 3d and g show the longterm cycling stability of the Li//SPE-IL//Li battery at a current density of 2.5 mA cm^{-2} and an area capacity of 0.5 mA h cm^{-2}. It was found that Li//SPE-IL//Li exhibited excellent cycling performance during the 200 hours of continuous platingstripping process. In Fig. 3d, the overpotential of the Li//LE//Li battery using liquid electrolytes continues to fluctuate, and an overpotential of nearly 300 mV is reached at 200 h. In contrast, the Li//SPE-IL//Li battery has a stable overpotential of only about 40 mV in 200 h. The high CCD value and excellent stability at high current density of the Li//SPE-IL//Li battery confirm that a stable interface can be formed between the SPE-IL and the lithium sheet. More importantly, high t_{Li^+} promotes the uniform and rapid deposition of lithium ions, and improves the tolerance of the Li//SPE-IL//Li battery at high current density.

The preparation process diagram of N(PDA)-CNT@S flexible self-supporting cathodes is shown in Fig. 4a. The carbon nanotube (CNT) film provides abundant adhesion sites, and the strong adhesion of the PDA achieves an in situ polymerization coating on the CNT surface.

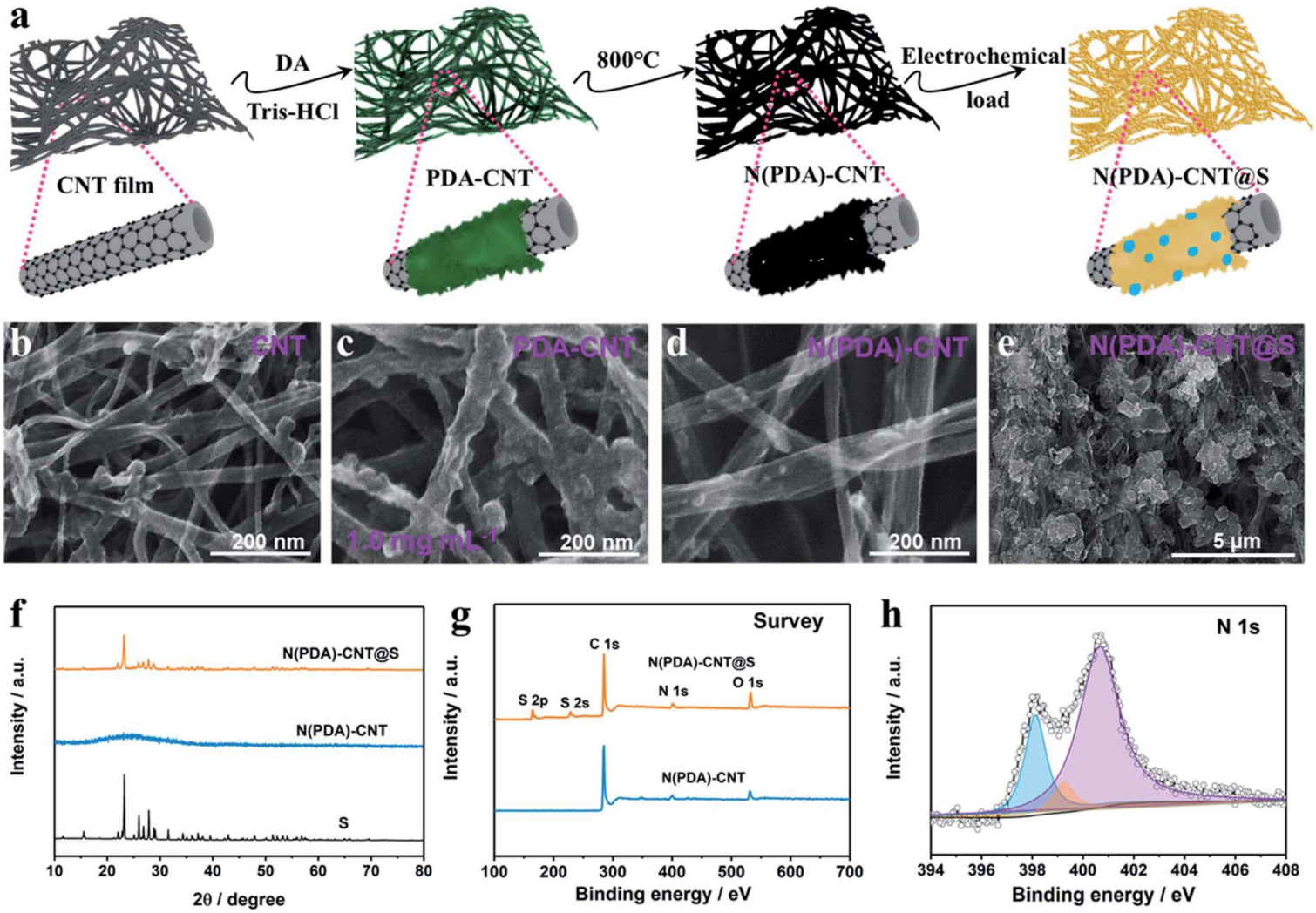

Fig. 4 (a) Schematic illustration of the formation of the N(PDA)-CNT@S composite film. FE-SEM images of the (b) CNT film, (c) PDA-CNT film, (d) N(PDA)-CNT film and (e) N(PDA)-CNT@S composite film. (f) XRD patterns and (g) XPS survey spectra of N(PDA)-CNT and N(PDA)-CNT@S. (h) N 1s XPS spectra of N(PDA)-CNT.

Until the DA concentration is 1.0 mg ml^{-1}, the CNTs no longer have an exposed surface for the PDA to attach, and the PDA coating amount reaches saturation (Fig. S12†). In addition, Fig. 4b, c and S13† show the comparison of the FE-SEM images of PDA-CNT with DA concentrations of 0, 0.2,1.0 and 1.4 mg mL^{-1}. It was found that the surface of the original CNT film in Fig. 4b was smooth with a diameter of about 20 nm. After coating PDA, the surface became rough. At DA concentrations of 1.0 mg mL^{-1} (Fig. 4c) and 1.4 mg mL^{-1} (Fig. S13bf), the diameter of the PDA-CNT increased significantly, about 50 nm. After that, the PDA-CNT was calcined at 800 °C to achieve nitrogen doping. It can be seen from Fig. 4d that the diameter of N(PDA)-CNT becomes significantly smaller, indicating that PDA decomposes after being carbonized at high temperature. Fig. S14† shows a balance between the electronic conductivity and the nitrogen doping. Considering comprehensively, 1 mg mL^{-1} was selected as the optimal concentration of DA. FTIR spectra (Fig. S15†) prove that DA monomers are polymerized onto the CNT surface.

After the electrochemical loading of sulfur, irregular particles appeared on the CNT surface (Fig. 4e). From the XRD patterns of S, N(PDA)-CNT, and N(PDA)-CNT@S (Fig. 4†), it can be seen that the sulfur powder has sharp diffraction peaks at multiple diffraction angles, indicating the crystal nature of elemental sulfur (JCPDS card no. 08-0247). For N(PDA)-CNT, the broad peak at 20-30° corresponds to the (002) crystal plane of the graphite carbon. After loading sulfur, the sharp diffraction peak of sulfur appeared in N(PDA)-CNT@S, which proved that the sulfur was successfully compounded with N(PDA)-CNT. In Fig. S16,† the characteristic bands of sulfur appear in the Raman spectrum of N(PDA)-CNT@S, which also proves the successful loading of sulfur.

The XPS survey spectra of N(PDA)-CNT and N(PDA)-CNT@S are shown in Fig. 4g. It can be seen that in addition to the C 1s, O 1s, and N 1s energy levels, N(PDA)-CNT@S has two peaks at 164.7 eV and 228.6 eV, which correspond to the S 2p and S 2s energy levels, respectively. As shown in Fig. 4h, the N 1s peak can be decomposed into three peaks with binding energies of 398.1, 400.6, and 403.8 eV, representing pyridine, pyrrole, and graphite nitrogen doped in the N(PDA)-CNT, respectively. In addition, the sulfur content measured using the TG curve (Fig. S17†) is 71%, and the average sulfur loading is 4.5 mg cm^{-2}.

Fig. 5a and d show the cyclic voltammetry curves (0.1 mV s-1) of SPE-IL-based quasi-solid-state lithium-sulfur batteries at different temperatures in the voltage range of 1.5 V to 3 V. It can be found that during the discharge process at room temperature, there are two reduction peaks at about 2.01 V and 1.86 V, which, respectively, correspond to the reduction of S_8 to the lithium polysulfide intermediate and the further conversion of the intermediate to Li_2S.

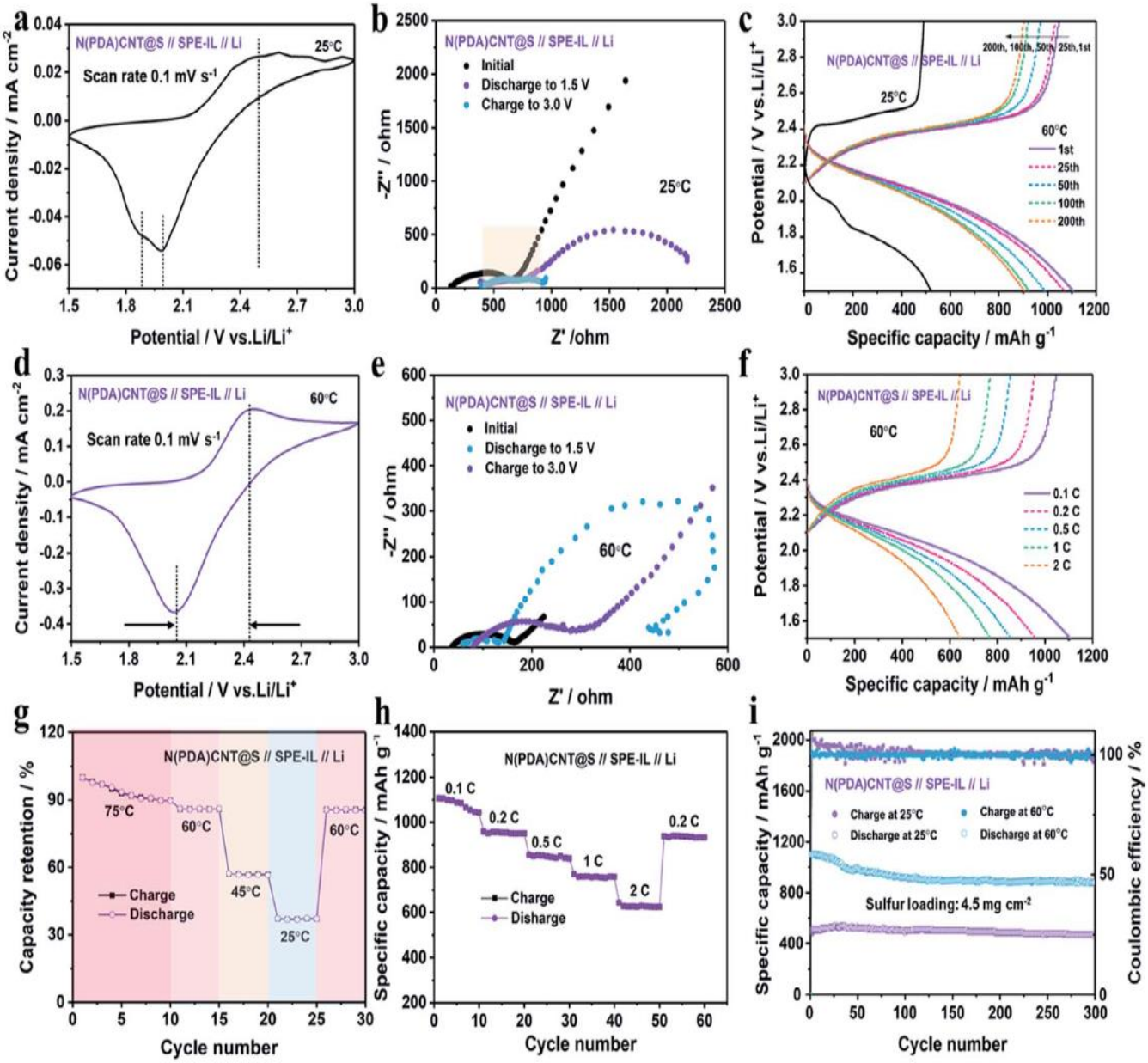

Fig. 5 Electrochemical performance of the N(PDA)CNT@S//SPE-IL//Li battery at different temperatures. CV curves at (a) 25 °C and (b) 60 °C. Nyquist plots under different voltages at (c) 25 °C and (d) 60 °C. Charge/discharge profiles at different (e) temperatures and (f) C-rates (60 °C). Rate performance at different (g) temperatures and (h) C-rates (60 °C). (i) Cycling performance at different temperatures.

This discharge method is similar to that of traditional ether-based liquid electrolyte lithium-sulfur batteries. The oxidation peak near 2.52 V is related to the conversion of Li_2S to S_8 during charging. Interestingly, when the temperature is raised to 60 °C, the two reduction peaks merged into one and appeared at 2.05 V. At the same time, the oxidation peak shifted to a lower potential (2.43 V). In addition, the peak current density at high temperature is an order of magnitude higher than that at room temperature, and all of these results indicate that the N(PDA)CNT@S//SPE-IL//Li battery exhibits excellent reversibility at high temperature.

The impedance spectra at different potentials in Fig. 5b and e further demonstrate this view. The introduction of ionic liquids reduced the impedance of the system by two orders of magnitude (Fig. S18†). At the room temperature of 25 °C, when the N(PDA)CNT@S//SPE-IL//Li battery was discharged

to 1.5 V, an additional semicircle was found in the low frequency region, which was related to the formation of Li_2S_2/Li_2S.[40] When continuously charged to 3 V, the semicircle in the low frequency region becomes smaller, but it can be seen from the partial enlarged view (Fig. S19†) that there are still two semicircles, which represent the irreversible conversion of solid Li_2S to lithium polysulfides.[40] At a high temperature of 60 °C, it was discharged to 1.5 V to perform impedance spectroscopy. Similarly, it was found that a semicircle appeared in the low frequency region, but the semicircle at 60 °C was larger, which means more Li_2S_2/Li_2S deposition. When continuously charged to 3 V, the semicircle in the low-frequency region completely disappears, which means that the battery has excellent reversibility at 60 °C. It can be seen from the charge and discharge curves (Fig. 5c) that there are two plateaus in the discharge curve at 25 °C, while the battery has only one discharge plateau at 60 °C, which is consistent with the CV results.

In addition to kinetics reversibility, the N(PDA)CNT@S//SPE-IL//Li battery also has good rate performance at 60 °C (Fig. 5f and h). When the current density is 0.2C, 0.5C, 1C and 2C, the discharge capacity is 959, 855, 770 and 643 mA h g^{-1}, respectively. When the current density returns to 0.2C again, it still has a specific capacity of 938 mA h g-1. This benefits from the introduction of dual Li-ion migration channels, which promotes ion conduction and accelerates the transmission of lithium ions, thereby improving the rate performance of the battery. In addition, Fig. 5g shows the rate performance of the N(PDA)CNT@S//SPE-IL//Li battery at different temperatures. It can be seen that when the temperature is as high as 75 °C, the capacity decays rapidly, and it shows good rate performance below 60 °C. Furthermore, Fig. 5i shows the cycling performance of the N(PDA)CNT@S//SPE-IL//Li battery at different temperatures. At room temperature, the first lap discharge capacity is 515 mA h g^{-1}. After 300 cycles, the discharge capacity is 445 mA h g^{-1}, and the capacity retention rate is 86.4%. The N(PDA)CNT@S//SPE-IL//Li battery at a working temperature of 60 °C can deliver a superior discharge capacity of 1106 mA h g^{-1} in the first cycle, which is consistent with the impedance results. The battery has more lithium sulfide deposition and higher capacity contribution at high temperature. After 300 cycles, the discharge capacity of N(PDA)CNT@S//SPE-IL//Li can still reach 887 mA h g^{-1}, the capacity retention rate is 80.2%, and the average capacity attenuation per cycle is only 0.066%.

In the discharge curve of the N(PDA)CNT@S//LE//Li battery using a traditional ether liquid electrolyte (Fig. 6a), two obvious discharge platforms represent the typical two-step reduction process of liquid lithium-sulfur batteries. The upper plateau and slopping region belong to the dissolution area of the long-chain lithium polysulfide Li_2Sn (n = 8-4), and the capacity contributed by this part is recorded as Q_1. The lower plateau is the precipitation area of the short-chain lithium polysulfide Li_2Sn (n = 2-1), and the capacity contributed by this part is recorded as Q_2. When the SPE-IL-based quasi-solid-state lithium-sulfur battery is discharged at 25 °C, the curve still has the characteristics of two-step reduction, but the platform has become less obvious. By calculating the Q_2/Q_1 value, we found that compared to that of the LE-based battery (1.81), the Q_2/Q_1 of the battery using the SPE-IL increased to 2.32. The increase of the capacity contribution ratio indicates that the deposition of lithium sulfide is dominant in the discharge process of the N(PDA)CNT@S//SPE-IL//Li battery at room temperature, and the contribution of capacity depends more on the deposition area of lithium sulfide. At 60 °C, the discharge curve of the SPE-IL based quasi-solid-state lithium-sulfur battery shows a one-step reduction process, which indicates that the conversion processes of S_8 to long-chain lithium polysulfide and long-chain lithium polysulfide to short-chain lithium polysulfide are combined as one. At this time, the time for which soluble lithium polysulfides exist in the system is greatly shortened, and the contribution of capacity depends entirely on the deposition of lithium sulfide. Due to the abundant ester groups in the SPE-IL, the irreversible shuttle of lithium polysulfides into the electrolyte can be effectively inhibited, and the high utilization rate of active substances can be ensured. EDS linear scanning of the SPE-IL before and after the cycling (Fig. 6c and d) showed that compared with the initial state, the sulfur

content in the electrolyte did not change significantly after 300 cycles, which proved that the SPE-IL successfully inhibited the irreversible dissolution of lithium polysulfides.

In order to understand the solid-solid interface evolution of the SPE-IL-based quasi-solid-state lithium-sulfur battery during the cycling process, the electrolytic cell shown in Fig. S20† was used to perform in situ optical imaging from the cross-section of the battery. The electrolyte is in close contact with the electrodes, and successfully lighted the diode (inset in Fig. 6b). It can be seen from Fig. 6b that when half of the battery is discharged to 1.5 V and then charged to 3 V at 60 °C, the high-modulus electrolyte successfully suppresses the volume deformation of the electrodes. In addition, the migration and shuttle of lithium polysulfides are not captured at the electrode-electrolyte interfaces, showing a high degree of reversibility. This is due to the strong chemical adsorption of lithium polysulfides by the abundant ester groups in the SPE-IL. In ATR-FTIR (Fig. S10†), the carbonate group in the electrolyte membrane after cycling has a red shift to 1809 cm^{-1} compared with the 1815 cm^{-1} of the initial state.

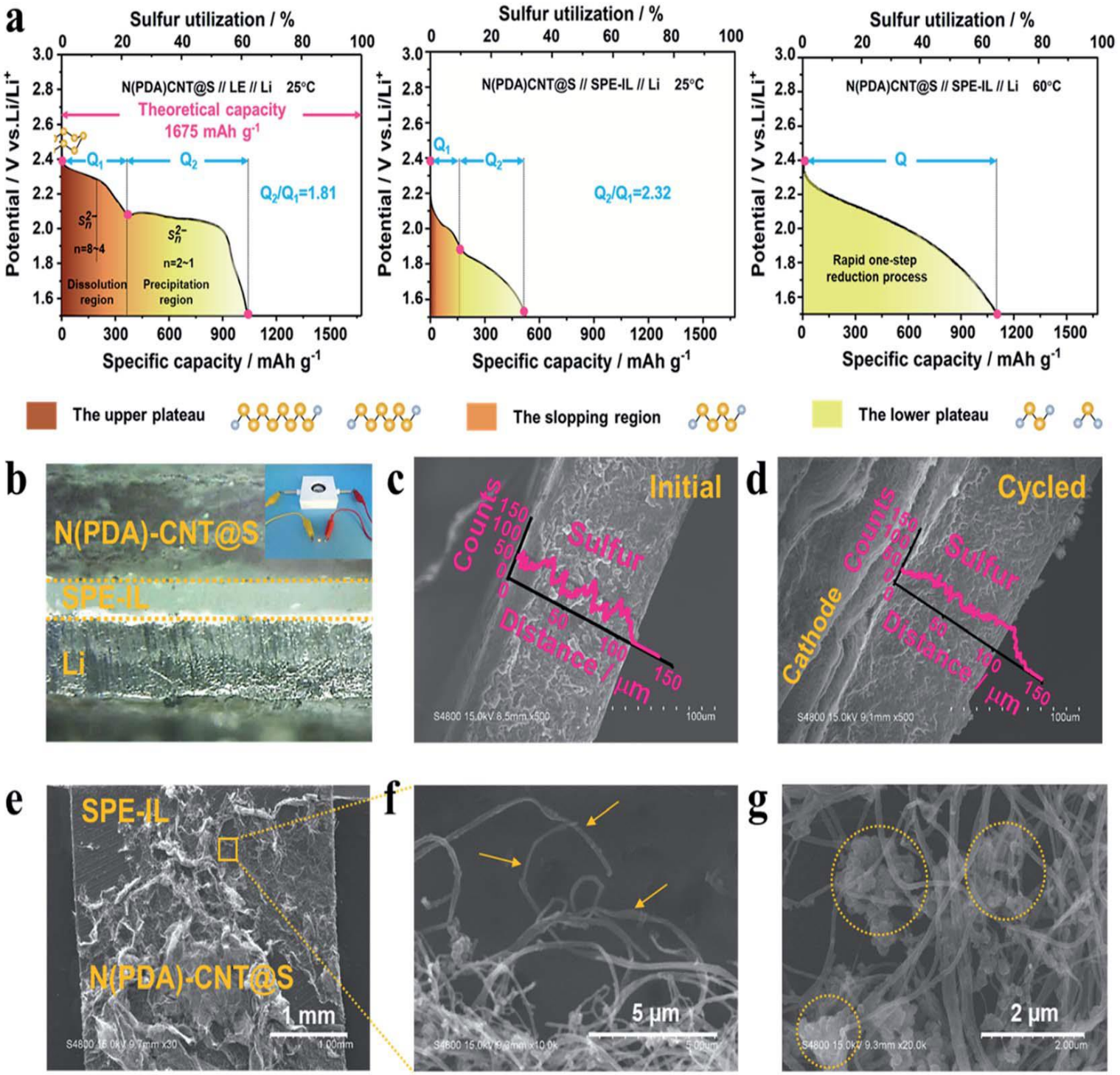

Fig. 6 (a) Study on discharge mechanisms of the N(PDA)CNT@S//LE//Li battery and N(PDA)CNT@S//SPE-IL//Li battery. (b) In situ optical imaging of the battery's cross-section and (inset) a digital photo of lighting the diode. (c and d) FE-SEM images of the SPE-IL (c) before and (d) after 300 cycles at 60 °C and the corresponding linear scanning EDS of sulfur. (e) FE-SEM image of difficult separation between the N(PDA)CNT@S cathode and SPE-IL, and (f) the corresponding partial enlarged image. (g) FE-SEM image of the N(PDA)CNT@S cathode after 300 cycles.

In the ^{7}Li NMR spectra (Fig. S21†), due to the coordination of the Li-O bond, the electron cloud density of Li atoms is reduced, which causes resonance under a lower electric field (chemical shift from -1.1 to -0.1 ppm). In addition, after cycling, the peak of the lithium atom becomes wider than that of the initial state, which also proves the chemical coordination between the SPE-IL and lithium polysulfides.

In order to explore the interfacial contact between the SPE-IL and N(PDA)CNT@S cathode, the SPE-IL-based quasi-solid-state lithium-sulfur battery was disassembled after 300 cycles at 60 °C. It is found in the FE-SEM image (Fig. 6e) that the N(PDA) CNT@S cathode and the electrolyte are tightly bonded together and cannot be peeled off. In the partial enlarged photo (Fig. 6f) and the cross-sectional photo (Fig. S22†), it is found that the close contact between the electrolyte and the cathode is achieved by a small part of the carbon nanotubes lapped inside the electrolyte. This contact mode can not only reduce the interface resistance, but also reduce the ion migration barrier. After 300 cycles, the active material sulfur is still firmly bound by the intricate entanglement structure of the carbon nanotube film (Fig. 6g).

References

1 M. Armand and J. M. Tarascon, Nature, 2008, 451, 652-657.

2 B. Dunn, H. Kamath and J. M. Tarascon, Science, 2011, 334, 928-935.

3 X. L. Ji, K. T. Lee and L. F. Nazar, Nat. Mater., 2009, 8, 500506.

4 S. Urbonaite, T. Poux and P. Novak, Adv. Energy Mater., 2015, 5, 1500118-1500137.

5 M. Zhang, W. Chen, L. Xue, Y. Jiao, T. Lei, J. Chu, J. Huang, C. Gong, C. Yan, Y. Yan, Y. Hu, X. Wang and J. Xiong, Adv. Energy Mater., 2020, 10, 1903008.

6 L. Huang, J. Li, B. Liu, Y. Li, S. Shen, S. Deng, C. Lu, W. Zhang, Y. Xia, G. Pan, X. Wang, Q. Xiong, X. Xia and J. Tu, Adv. Funct. Mater., 2020, 30, 1910375.

7 M. Zhao, B. Q. Li, X. Chen, J. Xie, H. Yuan and J. Q. Huang, Chem, 2020, 6, 3297-3311.

8 Y. Hu, W. Chen, T. Lei, Y. Jiao, J. Huang, A. Hu, C. Gong, C. Yan, X. Wang and J. Xiong, Adv. Energy Mater. , 2020, 10, 2000082.

9 M. Zheng, X. Cai, Y. Tan, W. Wang, D. Wang, H. Fei, P. Saha and G. Wang, Chem. Eng. J., 2020, 389, 124404.

10 W. Wang, D. Wang, G. Wang, M. Zheng and G. Wang, Adv. Energy Mater., 2020, 10, 1904026.

11 M. Li, J. E. Frerichs, M. Kolek, W. Sun, D. Zhou, C. J. Huang, B. J. Hwang, M. R. Hansen, M. Winter and P. Bieker, Adv. Funct. Mater. , 2020, 30, 1910123.

12 S. Zhou, J. Hu, S. Liu, J. X. Lin, J. Cheng, T. Mei, X. Wang, H. G. Liao, L. Huang and S. G. Sun, Nano Energy, 2020, 72, 104680.

13 A. Eftekhari and D. W. Kim, J. Mater. Chem. A, 2017, 5, 17734-17776.

14 W. J. Chen, B. Q. Li, C. X. Zhao, M. Zhao, T. Q. Yuan, R. C. Sun, J. Q. Huang and Q. Zhang, Angew. Chem., Int. Ed., 2020, 132, 10821-10834.

15 P. Joo Hyun Kim, K. Kim and V. G. Pol, Carbon, 2018, 131, 175-183.

16 J. Li, L. Zhang, F. Qin, B. Hong, Q. Xiang, K. Zhang, J. Fang and Y. Lai, J. Power Sources, 2019, 442, 227232.

17 Z. Xiao, Z. Li, X. Meng and R. Wang, J. Mater. Chem. A, 2019, 7, 22730-22743.

18 Z. Zhou, B. Chen, T. Fang, Y. Li, Z. Zhou, Q. Wang, J. Zhang and Y. Zhao, Adv. Energy Mater., 2020, 10, 1902023.

19 Z. Li, W. Lu, N. Zhang, Q. Pan, Y. Chen, G. Xu, D. Zeng, Y. Zhang, W. Cai, M. Yang, Z. Yang, Y. Sun, H. Ke and H. Cheng, J. Mater. Chem. A, 2018, 6, 14330-14338.

20 X. Gai, B. Cui, B. Ye, W. Wang, J. Ding and G. Wang, ACS Appl. Mater. Interfaces, 2019, 11, 38136-38146.

21 T. Jiang, P. He, G. Wang, Y. Shen, C. W. Nan and L. Z. Fan, Adv. Energy Mater., 2020, 10, 1903376.

22 Z. Wu, Z. Xie, A. Yoshida, X. An, Z. Wang, X. Hao, A. Abudula and G. Guan, Chem. Eng.J., 2020, 380, 122419.

23 D. Shao, L. Yang, K. Luo, M. Chen, P. Zeng, H. Liu, L. Liu, B. Chang, Z. Luo and X. Wang, Chem. Eng. J., 2020, 389, 124300.

24 S. Wang, P. Xiong, J. Zhang and G. Wang, Energy Storage Mater., 2020, 29, 310-331.

25 Y. Wang, G. Wang, P. He, J. Hu, J. Jiang and L. Z. Fan, Chem. Eng.J., 2020, 393, 124705.

26 J. Hu, P. He, B. Zhang, B. Wang and L. Z. Fan, Energy Storage Mater. , 2020, 26, 283-289.

27 J. H. Jiang, A. B. Wang, W. K. Wang, Z. Q. Jin and L. Z. Fan, J. Energy Chem., 2020, 46, 114-122.

28 Q. Yang, N. Deng, J. Chen, B. Cheng and W. Kang, Chem. Eng. J., 2020, DOI: 10.1016/j.cej.2020.127427.

29 Z. Liu, X. He, C. Fang, L. E. Camacho-Forero, Y. Zhao, Y. Fu, J. Feng, R. Kostecki, P. B. Balbuena, J. Zhang, J. Lei and G. Liu, Adv. Funct. Mater., 2020, 30, 2003605.

30 L. Chen, Y. Li, S. P. Li, L. Z. Fan, C. W. Nan and J. B. Goodenough, Nano Energy, 2018, 46, 176-184.

31 Y. Liu, B. Xu, W. Zhang, L. Li, Y. Lin and C. Nan, Small, 2020, 16, 1902813.

32 N. Ahmad, L. Zhou, M. Faheem, M. K. Tufail, L. Yang, R. Chen, Y. Zhou and W. Yang, ACS Appl. Mater. Interfaces, 2020, 12, 21548-21558.

33 M. K. Tufail, L. Zhou, N. Ahamd, R. Chen, M. Faheem, L. Yang and W. Yang, Chem. Eng. J., 2020, 407, 127149.

34 A. K. Kenessova, G. A. Seilkhanova, T. S. Kurmanbayeva, E. Z. Ussipbekova and A. P. Kurbatov, Mater. Today: Proc., 2020, 31, 588-591.

35 P. Chiochan, X. Yu, M. Sawangphruk and A. Manthiram, Adv. Energy Mater., 2020, 10, 2001285.

36 J. P. Mwizerwa, Q. Zhang, F. Han, H. Wan, L. Cai, C. Wang and X. Yao, ACS Appl. Mater. Interfaces, 2020, 12, 1851918525.

37 X. Li, D. Wang, H. Wang, H. Yan, Z. Gong and Y. Yang, ACS Appl. Mater. Interfaces, 2019, 11, 22745-22753.

38 L. P. Hou, H. Yuan, C. Z. Zhao, L. Xu, G. L. Zhu, H. X. Nan, X. B. Cheng, Q. B. Liu, C. X. He, J. Q. Huang and Q. Zhang, Energy Storage Mater., 2020, 25, 436-442.

39 S. Lou, F. Zhang, C. Fu, M. Chen, Y. Ma, G. Yin and J. Wang, Adv. Mater. , 2020, DOI: 10.1002/adma.202000721.

40 Y. X. Song, Y. Shi, J. Wan, S. Y. Lang, X. C. Hu, H. J. Yan, B. Liu, Y. G. Guo, R. Wen and L. J. Wan, Energy Environ. Sci., 2019, 12, 2496-2506.

41 P. Zhu, C. Yan, J. Zhu, J. Zang, Y. Li, H. Jia, X. Dong, Z. Du, C. Zhang, N. Wu, M. Dirican and X. Zhang, Energy Storage Mater. , 2019, 17, 220-225.

42 X. Chen, L. Yuan, Z. Li, S. Chen, H. Ji, Y. Qin, L. Wu, Y. Shen, L. Wang, J. Hu and Y. Huang, ACS Appl. Mater. Interfaces, 2019, 11, 29830-29837.

43 L. Fan, S. Chen, J. Zhu, R. Ma, S. Li, R. Podila, A. M. Rao, G.Yang, C. Wang, Q. Liu, Z. Xu, L. Yuan, Y. Huang and B. Lu, Adv. Sci., 2018, 5, 1700934.

44 J. Liu, T. Qian, M. Wang, J. Zhou, N. Xu and C. Yan, Nano Lett., 2018, 18, 4598-4605.

45 Z. Fan, B. Ding, T. Zhang, Q. Lin, V. Malgras, J. Wang, H. Dou, X. Zhang and Y. Yamauchi, Small, 2019,15,1903952.

46 Y. Xia, Y. F. Liang, D. Xie, X. L. Wang, S. Z. Zhang, X. H. Xia, C. D. Gu and J. P. Tu, Chem. Eng.J., 2019, 358, 1047-1053.

47 L. Luo and A. Manthiram, Energy Technol., 2020, 8, 2000348.

48 L. Chen and L. Z. Fan, Energy Storage Mater., 2018,15, 37-45.

49 H. Zhao, N. Deng, J. Yan, W. Kang, J. Ju, Y. Ruan, X. Wang, X. Zhuang, Q. Li and B. Cheng, Chem. Eng. J., 2018, 347, 343-365.

50 Y. Y. Liu, D. Lin, P. Yuen, K. Liu, J. Xie, R. H. Dauskardt and Y. Cui, Adv. Mater., 2017, 29, 1605531.

51 M. Yan, W. P. Wang, Y. X. Yin, L. J. Wan and Y. G. Guo, EnergyChem, 2019, 1, 100002.

52 M. Zhao, B. Q. Li, H. J. Peng, H. Yuan, J. Y. Wei and J. Q. Huang, Angew. Chem., Int. Ed., 2020, 59, 12636-12652.

53 J. Chai, Z. Liu, J. Zhang, J. Sun, Z. Tian, Y. Ji, K. Tang, X. Zhou and G. Cui, ACS Appl. Mater. Interfaces, 2017, 9,17897-17905.

54 Z. Tu, P. Nath, Y. Lu, M. D. Tikekar and L. A. Archer, Acc. Chem. Res., 2015, 48(11), 2947-2956.

55 C. Fu, V. Venturi, J. Kim, Z. Ahmad, A. W. Ells, V. Viswanathan and B. A. Helms, Nat. Mater., 2020, 19, 758-766.

56 Y. Wang, Y. Pan and D. Kim, Polym. Int., 2007, 56, 381-388.

57 Z. Liao, J. Huang, W. Chen, N. Saito, Z. Zhang, L. Yang and S. i. Hirano, Energy Storage Mater., 2020, 33, 442-451.

58 K. M. Diederichsen, H. G. Buss and B. D. McCloskey, Macromolecules, 2017, 50, 3831-3840.

59 J. Chai, Z. Liu, J. Ma, J. Wang, X. Liu, H. Liu, J. Zhang, G. Cui and L. Chen, Adv. Sci., 2017, 4, 1600377.

60 Z. Liu, W. Zhou, C. Wang, W. Hu and Z. Chen, J. Sep. Sci., 2020, 43, 2827-2833.

61 H. Tokuda, K. Hayamizu, K. Ishii, M. A. B. H. Susan and M. Watanabe, J. Phys. Chem. B, 2005, 109, 6103-6110.

62 Y. M. Xie, B. Yu, C. Ma, X. Xu, Y. Cheng, S. Yuan, Z. Wang, H. T. Chandran, C. S. Lee, L. S. Liao and S. W. Tsang, J. Mater. Chem. A, 2018, 6, 9081-9088.

63 O. Nordness and J. F. Brennecke, Chem. Rev., 2020, 120, 12873-12902.

64 J. Chai, J. Zhang, P. Hu, J. Ma, H. Du, L. Yue, J. Zhao, H. Wen, Z. Liu, G. Cui and L. Chen, J. Mater. Chem. A, 2016, 4, 51915197.

65 K. Ito, N. Nishina and H. Ohno, J. Mater. Chem., 1997, 7, 1357-1362.

66 F. Lu, Y. Pang, M. Zhu, F. Han, J. Yang, F. Fang, D. Sun, S. Zheng and C. Wang, Adv. Funct. Mater., 2019, 29,1809219.